Characterising the heat and mass transfer coefficients for a crossflow interaction of air and water

Reza Enayatollahi*, Roy Jonathan Nates, Timothy Anderson
Department of Mechanical Engineering, Auckland University of Technology, Auckland, New Zealand.
Corresponding Author: Reza Enayatollahi
Email Address: renayato@aut.ac.nz
Postal Address: WD308, 19 St Paul Street, Auckland CBD, Auckland, New Zealand
Phone Number: +64 9 921 9999 x8109

Abstract

An experimental study was performed in order to characterise the heat and mass transfer processes, where an air stream passes through a sheet of falling water in a crossflow configuration. To achieve this, the hydrodynamics of a vertical liquid sheet in a ducted gaseous crossflow were studied. Four distinct flow regimes were identified (a stable sheet, a broken sheet, a flapping sheet and a lifted sheet) and mapped using Reynolds and Weber numbers. Subsequently, the Buckingham π theorem and a least squares analyses were employed leading to the proposal of two new dimensionless numbers referred to as the Prandtl Number of Evaporation and the Schmidt Number of Evaporation. These describe the heat and mass transfer in low temperature evaporation processes with crossflow interaction. Using these dimensionless numbers, empirical correlations for Sherwood and Nusselt numbers for the identified flow regimes were experimentally determined. These correlations were in a good agreement with their corresponding experimental values. It was found that flapping sheets have the strongest heat and mass transfer intensities whereas the weakest intensities were seen for the "stable" sheets.

Keywords: Heat and mass transfer, Flow regimes, Crossflow, Liquid sheet, Gas stream

Nomenclature

A	Area (m^2)
c_p	Specific heat ($J/kg.K$)
$\hbar$	Enthalpy (J/kg)
h	Heat transfer coefficient ($W/m^2.K$)
j	Mass transfer coefficient (m/s)
k	Thermal conductivity ($W/m.K$)
L	Length (m)
$\dot{m}$	Mass flow rate (kg/s)
P	Pressure (kPa)
Q	Flow rate per unit length (m^2/s)
$\dot{Q}$	Rate of heat transfer (W)
R	Specific gas constant ($J/kg.K$)
T	Temperature (K)
V	Velocity (m/s)
μ	Viscosity ($kg/m.s$)
λ	Mass diffusivity (m^2/s)
ρ	Density (kg/m^3)
σ	Surface tension(N/m)
ω	Specific humidity ($kg_{water}/kg_{dry\ air}$)

Subscripts

∞	Bulk fluid
a	Air
ch	Characteristic
$Conv$	Convection
ev	Evaporation
ev	Evaporation
f	Film
fg	Vaporization
in	Inlet
loc	Local
m	Mean
noz	Nozzle
out	Outlet
R	Resultant
t	Total
v	Vapour
w	Water

1. Introduction

Heat and mass transfer devices involving liquid and gas streams interacting have a wide range of applications including distillation plants, cooling towers, aeration processes and desiccant drying [1-5]. Enhancing the heat and mass transfer processes in these systems could improve the overall performance, and reduce the size and cost of these devices.

In this respect, the nature of the flow and the interaction of the phases has a significant influence on the heat and mass transfer processes. In order to be able to design a simultaneous heat and mass exchanger, a developed non-dimensional understanding of heat and mass transfer processes for the possible modes of interaction is required. A number of investigations have sought to characterise the heat and mass transfer processes for different applications, in different geometries and conditions of interactions [6-10]. For example, Wee et al. [11], performed an investigation on simultaneous natural convection heat and mass transfer in a vertical and horizontal cavity. It was reported that the Nusselt and Sherwood numbers were functions of the Rayleigh number only for both the horizontal and vertical cavities. Iskra et al. [12], determined the convective mass transfer coefficient for evaporation in a horizontal rectangular duct. The experimental Sherwood number for both laminar and turbulent flows was reported as a function of the Rayleigh and Graetz numbers and the Nusselt number was derived from the Chilton-Colburn analogy.

Extending this to forced convection, Sun et al. [13], theoretically and experimentally examined the heat and mass transfer processes for drying a short porous cylinder. It was reported that both the Nusselt and Sherwood numbers are functions of the Reynolds and Gukhman numbers, in which Gukhman number expresses the ratio of the outer mass transfer intensity to the outer heat transfer intensity. Chuck et al. [14] studied the evaporative mass and heat transfer from a partially filled pan of water situated in the floor of a rectangular duct with turbulent air flow. It was reported that the Sherwood number was a function of the Reynolds number of the air stream and the aspect ratio of the unfilled portion of the water pan. It was also shown that the Nusselt number could be determined using the analogy between heat and mass transfer.

Now for this work the aim was to develop an understanding of a crossflow interaction, where gas stream flows horizontally through falling sheets of liquid, and how this influences the intensities of heat and mass transfer, with particular reference to improving the performance of a solar desalination system [1]. Although there has been extensive work on characterising the heat and mass transfer in different configurations, there are no studies that characterise the intensities of heat and mass transfer when falling sheets are exposed to a gas crossflow.

Now, given the complexity of such an interaction, and the absence of simple analytical solutions, it is necessary to provide a flow regime map to aid the design of heat and mass transfer devices involving falling liquids in gaseous crossflows. Numerous studies have examined the behaviour of sheets of falling liquid, in quiescent gas, [15-21] and similarly a number of studies have examined the behaviour of liquid sheets with gas co-flow and around jets in crossflow [22-24]. Bolanos-Jimenez et al. [25] performed a theoretical and experimental study on the behaviour of air and water sheets in a parallel flow condition. They observed a “bubbling” regime that lead to the periodic breakup of the air sheet, and a “jetting” regime, where both sheets evolved slowly downstream without breaking. They suggested the formation

of either of these regimes was dependent on two factors, namely; the Weber number of the water and the velocity ratio between the air and the water.

Ng et al. [26] performed an experimental investigation on what they termed “bag breakup” of a circular, non-turbulent liquid jet with a gaseous crossflow. They found that as a result of gaseous crossflow a series of column waves would be formed in the jet flow and that the variable wave frequency caused instability. Based on their findings it is apparent that the primary breakup processes are due to the aerodynamic effects of the crossflow, regardless of initial disturbances within a liquid jet.

Extending this to liquid sheet flows, Brown [27] investigated the behaviour of a thin sheet of liquid exiting a slot and impinging on a moving solid surface. In this study it was reported that the liquid sheet would be unstable in the region close to the slot unless the liquid velocity outside the slot was greater than 2T/Q, where T is the surface tension of the liquid and Q is the mass flow rate. Using the Weber number, it was found that the sheet was stable for Weber numbers greater than unity. Becerra et al. [28] also performed an experimental study on the stability of a viscoelastic liquid sheet and reported that the liquid sheet would be unstable for Weber numbers below 0.94. They also noted that liquids with high extensional viscosity were able to create a more stable sheet.

Despite the work that has been undertaken on understanding falling liquid sheet flows and circular liquid jets in crossflow, there are no studies that examine the behaviour of falling liquid sheets when exposed to a gas crossflow and none that characterise the heat and mass transfer coefficients for such a process. Therefore, this work aims to experimentally characterise and map the flow regimes in such interactions and from this develop correlations to describe the heat and mass transfer.

2. Experimental Method

In order to develop an understanding of the behaviour of liquid sheets with a gas crossflow, an experiment was developed where a thin sheet of water was injected into a rectangular air channel, as shown in Figure 1. The sheet was generated by passing water through a slotted nozzle, formed by two finely grounded stainless steel plates. An elevated water reservoir was used to provide a constant head to the jet, where the height of this reservoir was adjustable in order to deliver a range of steady flow rates. The water flow rate was determined by measuring the time taken for a known mass of water to pass through the nozzle.

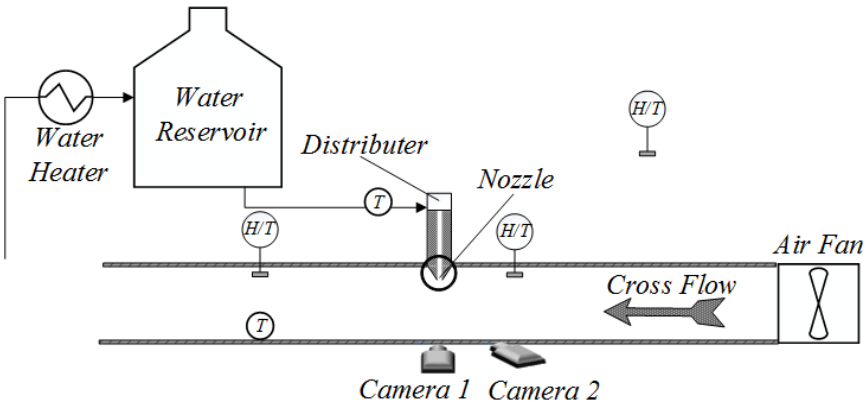

Figure 1. Experimental apparatus

To provide the crossflow, air was directed through the duct by a variable speed axial flow fan with a maximum capacity of 280 m^3/hr. The dimensions of the duct were a width of 100 *mm* and a height adjustable between 30 and 100 *mm*. For each test the airflow rate was determined from measurements made using a pitot static probe traversed across the duct and a differential manometer. Two cameras (*Nikon D300* and *Nikon D3300*) were used to capture images of the air and water interaction. The first of these (Camera 1) was mounted to capture a side elevation image while the second (Camera 2) was utilised to capture a profile image of the water sheet.

More importantly, to measure the heat and mass transfer, a set of three humidity/temperature sensors, (Sensirion SHT71) with an accuracy of ±0.3% for relative humidity and ±0.4 $^{\circ}C$ for temperature at standard room condition were used. As seen in Figure 1, sensors were placed on either side of the sheet to measure the change in humidity and temperature of the air stream, and the third one was placed outside the experimental set up to monitor the room conditions. The data from these sensors were logged using a Sensirion evaluation kit (EK-H4). Additionally, a set of two thermocouples (type T) with an accuracy of ±0.3 $^{\circ}C$ and a PicoLog (TC08) data logger were used to record the change in water temperature. Finally, an auxiliary water heater was used to control the inlet water temperature.

During the experiment, the effects of variation of air and water flow rates, as well as the inlet water temperature and channel height were evaluated. The inlet air temperature and humidity were not controlled in the experiment, but carefully monitored. The properties of air and water were determined for the conditions of each test, which the properties of pure water were considered for simplicity. The system pressure was also not controlled, but the atmospheric pressure was measured by a mercury barometer (*Griffin & Sons*).

3. Results: characterisation of flow regimes

The behaviour of falling sheets of water in a crossflow configuration was studied at various flow rates in a range of airflow rates with two different fall height and constant nozzle dimensions. Table 1 shows the experimental conditions.

Table 1. Experimental conditions for the observation of water sheets in air crossflow

Nozzle width	(m)	*0.1*
Nozzle thickness	(m)	*0.0005*
Air flow rate	(m^3/s)	0.42×10^{-2} *to* 2×10^{-2}
Water flow rate	(m^3/s)	2×10^{-5} *to* 5×10^{-5}
Air temperature	($^{\circ}C$)	*20*
Air humidity	(-)	*0.50*
Water temperature	($^{\circ}C$)	*15*
Fall height	(m)	*0.036 ; 0.048*

By altering the water flow rate, at various airflow rates, four different modes of interaction were found for the range of conditions tested, as illustrated in Figure 2. A “Broken sheet” is shown in Figure 2 (a-b) which was formed at higher flow rates of air and low flow rates of water. At lower airflow rates, regardless of water flow rate, the water sheet was observed to be “stable”, as shown in Figure 2 (c-d). High flow rates of air and high flow rates of water resulted in formation of a “flapping sheet”, shown in Figure 2 (e-f). Further increasing the airflow at higher flow water rates formed a “stable lifted sheet”, shown in Figure 2 (g-h).

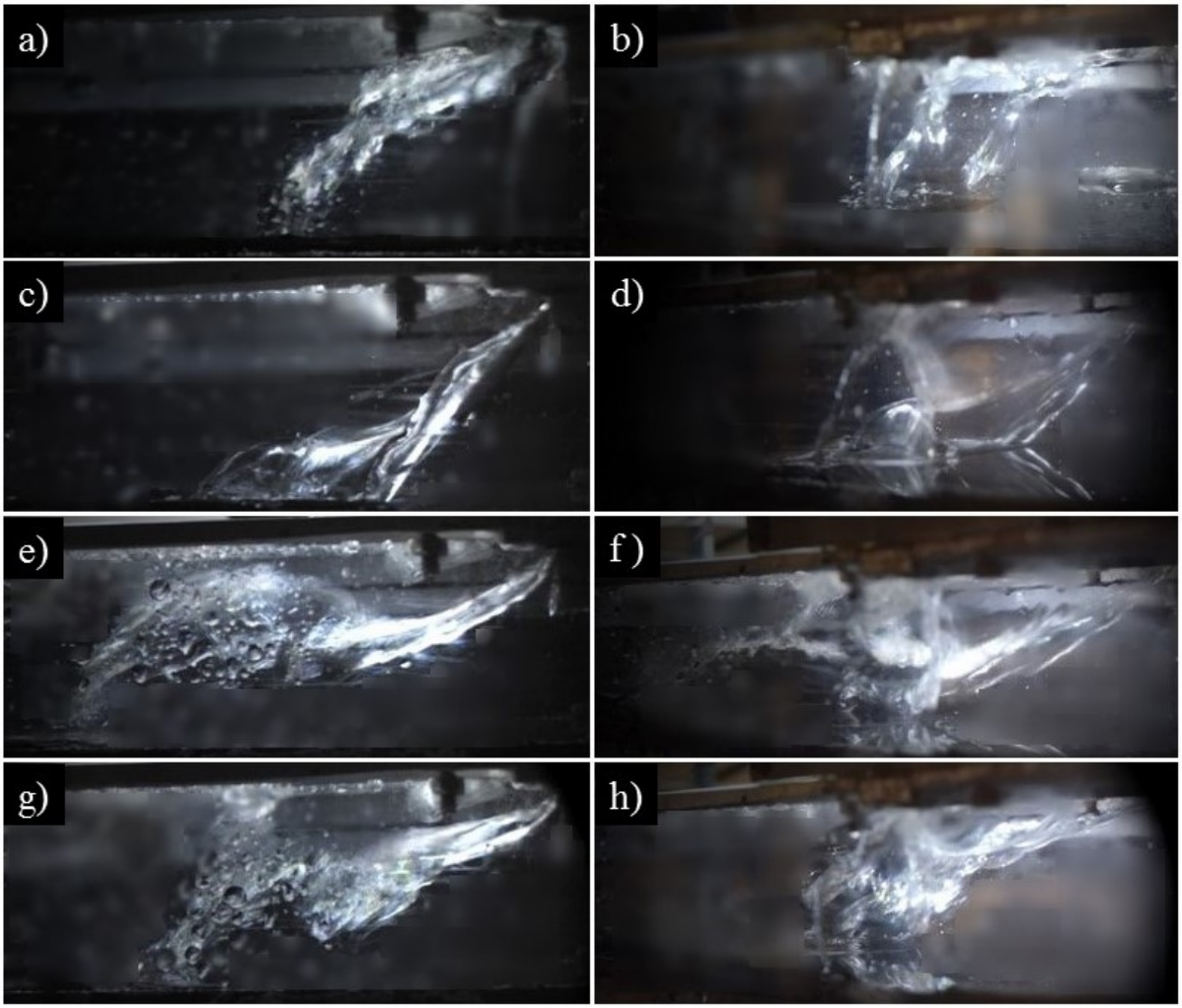

Figure 2. Water flow regime in air crossflow

The air crossflow exerts a pressure difference across the sheet as well as aerodynamic drag forces, which holds the water sheet at an angle to the horizontal. The pressure difference across the sheet causes the sheet to bow, pushing out the centre and dragging in the sides. Increasing the water flow rate on the other hand, increases the inertia of water, which attempts to "hold" the flow vertically. But also increases the area of the water sheet and thereby the drag forces. Depending on the blockage ratio (the ratio of the sheet area to the cross-sectional area of the channel) a portion of the air passes by the sheet with no significant effect on the water flow regime as illustrated in Figure 3.

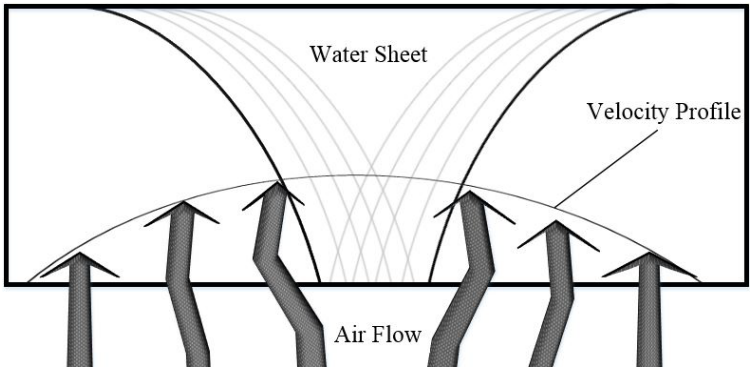

Figure 3. Behaviour of airflow in contact with a relatively small water sheet

Within the water sheet, the surface tension attempts to hold the water sheet together, however, once the drag forces dominate the internal cohesion, the water sheet breaks. It was found that if the velocity distribution in the sheet and hence the thickness of the water sheet is uniform, the sheet breaks up at the tail end of the sheet, as illustrated in Figure 2(e-f). Alternatively, as demonstrated in Figure 2(a-b), if the velocity profile is not uniform it breaks up vertically. In the following sections, the observed modes are explained in detail.

3.1. Stable Sheet

Depending on the fall height and the velocity of water at the nozzle, the geometry of the stable sheets was seen to be shaped like a “Y”, triangular or trapezoidal. At relatively low water flow rates and higher fall heights, the edges of the sheet meet each other above the bottom of the channel creating a Y sheet. By increasing the air crossflow on a stable sheet the drag due to the air initially inclines the falling water sheet and creates a concave arch in the middle of the sheet, as illustrated in Figure 4.

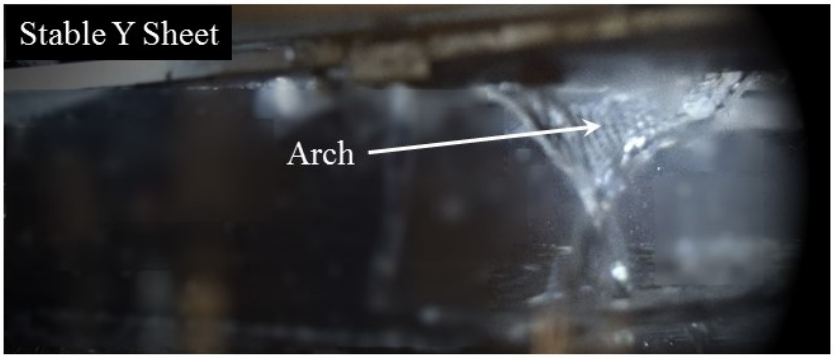

Figure 4. Stable Y Sheet

Increasing the water jet velocity increases the inertia of the water stream which increases the sheet area. This also increases the momentum of water stream which, as shown in Figure 5(a-f), pushes the arch down towards the bottom of air tunnel until it forms a water tunnel.

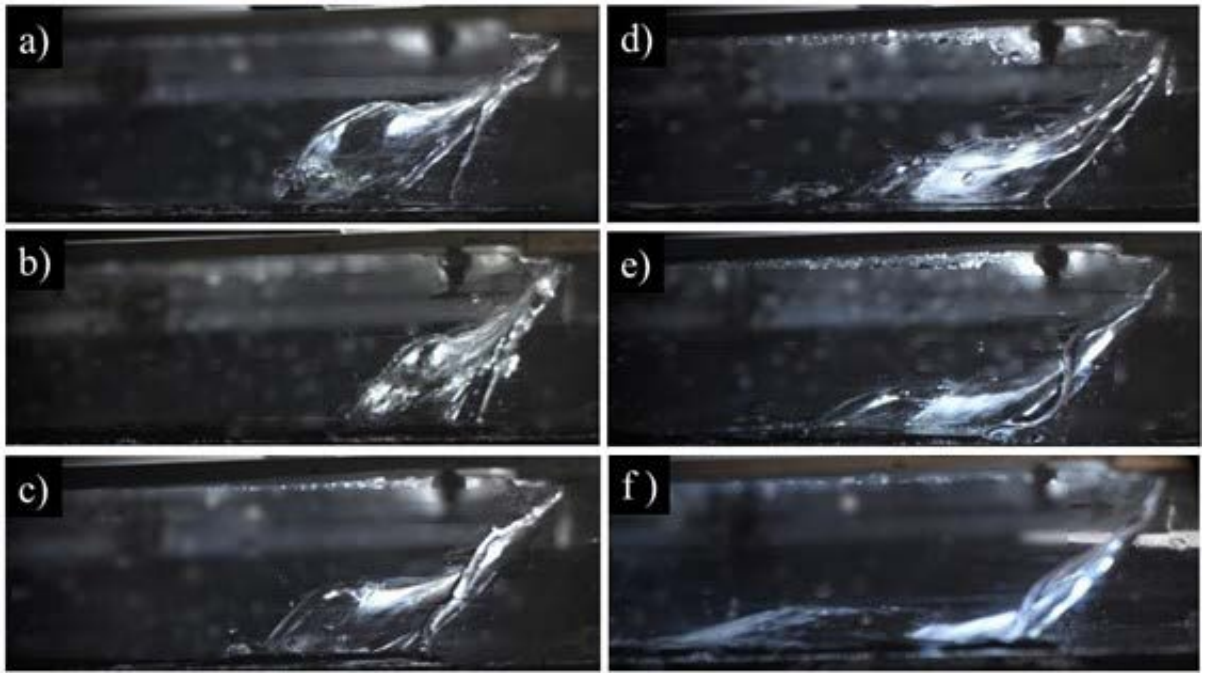

Figure 5. Position and shape of the arch at increased water flow rate and constant airflow

As a consequence of the small blockage ratio in Y sheets, the drag forces on these sheets are relatively small and therefore higher airflow rates are required to break up the sheet. However, the larger blockage ratio for triangular and trapezium geometries results in higher drag forces. Therefore, at higher water velocities the sheet will change its mode with lower flow rates of air in the duct. In this respect, the inclination angle of the sheet depends on the blockage ratio and the drag force, so that at smaller blockage ratios the inclination angle is smaller. On the other hand, increasing the water velocity increases the momentum of water in the vertical direction which attempts to reduce the inclination angle. Counter to this, increasing the air velocity in the duct has the effect of thinning the sheet due to the drag, thereby increasing the size of the concave arch until it eventually breaks up or moves to a flapping mode.

3.2. Broken Sheet

Broken sheets can be generated from either flapping or stable sheets by either increasing the air velocity at low water flow rates or reducing the water flow at high airflow rates. Due to the wall effects, the velocity of air is higher at the centre causing a shear stress across the sheet. At the same time, at lower water flow rates thinning occurs closer to the jet exit. Hence, once the sheet is relatively thin and the shear stress due to the airflow is strong enough to overcome the surface tension and inertia of the water stream, the sheet will break up vertically into fingers or smaller sheets, as shown in Figure 6(a-f).

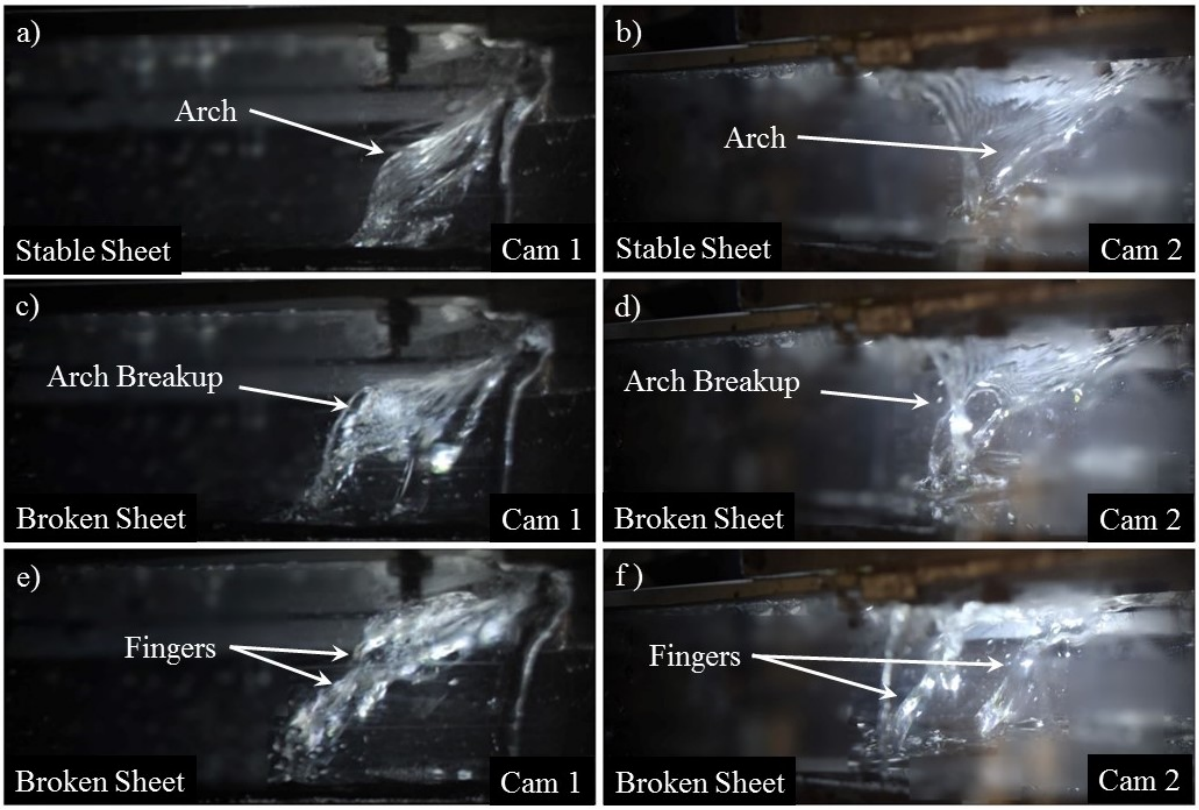

Figure 6. Break up of a triangular sheet into fingers by increasing the Reynolds number.

After break up, surface tension acts to pull the edges of these disjointed flows towards their centres, in order to minimise the surface area of the water sheet. This eventually thickens each individual flow to form the fingers, that reduce the contact area between the air and water sheet. As a consequence, the drag force on the water flow will be smaller and result in a smaller inclination angle.

By further increasing the airflow at a fixed water flow rate or decreasing the water flow at a fixed airflow rate, the fingers will break into droplets. This can be explained by the water flow accelerating in an inclined direction as a result of the gravitational and drag forces. As the water accelerates, the cross section of the water fingers decreases due to continuity and eventually, surface tension will break the fingers into droplets in order to bring the water flow into its minimum energy state.

3.3. Flapping and Stable Lifted Sheet

Once the velocity of water stream at the nozzle is high enough, such that the sheet thins only slightly as it falls, the sheet would resist breaking vertically. Under these conditions, if there is sufficient momentum in the air stream, the pressure drop and drag across the sheet is able to lift the sheet as a whole, as illustrated in and Figure 7. Once the sheet is lifted almost horizontally, the tail end of the sheet breaks into droplets, due to the continued acceleration of the water in the near horizontal plain. The lifting of the sheet, unblocks the channel and thus reduces the pressure drop across the sheet, hence, due to gravitational forces, the sheet falls back across the channel and repeats the process. This oscillation, named here as a “flapping sheet”, shown in Figure 7 (c-d), has the added effect of intermittently breaking off the tail of the sheet as it is flicked from the near vertical to horizontal position.

At high enough air velocities, there is sufficient momentum in the air to balance the gravity and hold the sheet with an inclination angle and the flapping will cease. As expected, the inclination of the sheet was higher with greater airflows. At these conditions, the airflow pushes the edges of the water flow towards the centre of the air channel. Hence, this mode is referred to as a “stable lifted sheet”. Figure 7 (a-f) shows the transformation of the stable sheet (a-b) to flapping sheet (c-d), and finally to a stable lifted sheet (e-f) at a constant water flow by altering the airflow rate.

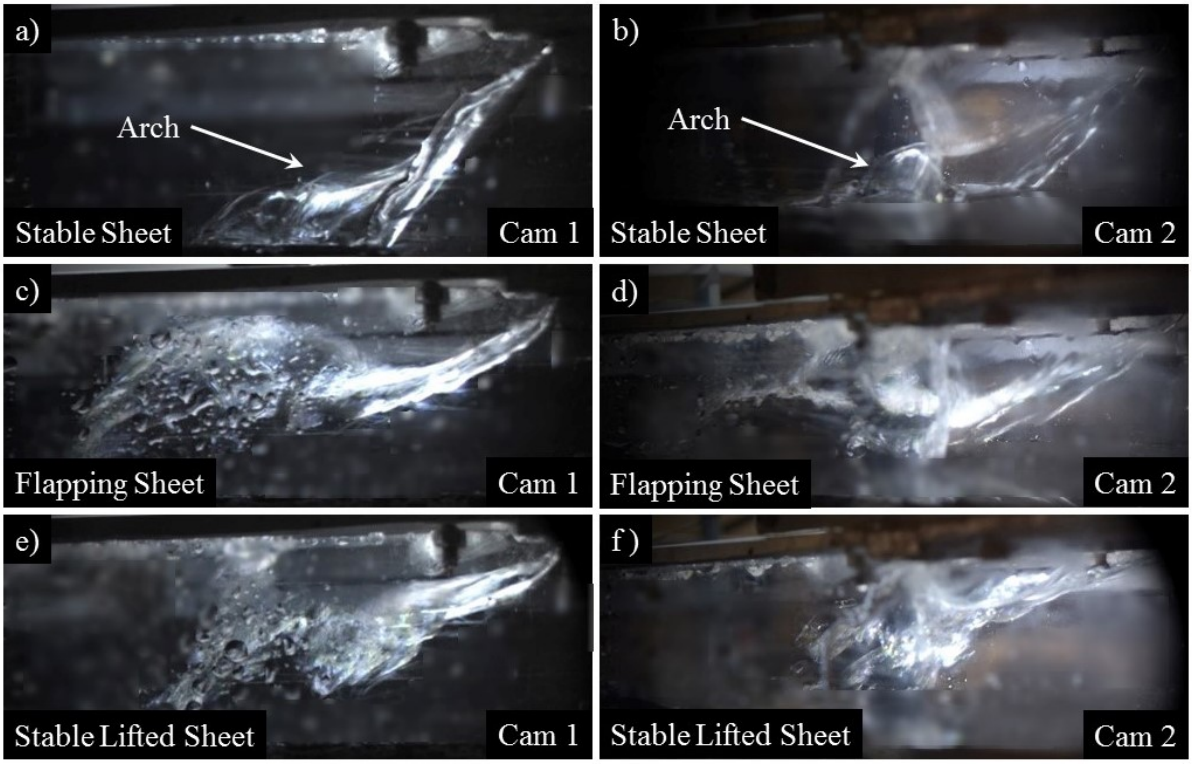

Figure 7.Transformation of the flow regime from stable sheet (a-b) to flapping sheet (c-d) and to stable merged flow (e-f).

3.4. Flow Regime Mapping

Flow regime maps are a graphical tool used to define the boundaries between different types of flow regimes in a specific system. These are based on the parameters that best describe the system. Many types of flow regime maps have been proposed for various geometries and conditions [29-32]. When describing a falling liquid in stagnant gas, the Weber number, defined as the ratio of inertia to surface tension, is often used to characterise the flow [25, 27, 28]. Considering the gas flow, Reynolds number, defined as the ratio of inertia and viscous forces, is often used to describe the characteristics of gas flow in a channel [33].

Hence, when a horizontal ducted airflow interacts with falling sheets of water, the characteristics of the water sheet can be described by its Weber number, and the response of the sheet to airflow can be dependent on the Reynolds number of the airflow. Therefore, it was decided to map the flow regimes according to the Weber number of the water (We_w), shown in Equation 1, and the Reynolds number of air (Re_a), given in Equation 2.

$$We_w = \frac{\rho_w {V_{ch,w}}^2 L_{ch,w}}{\sigma} = \frac{\rho_w V_{ch,w} Q_w}{2\sigma} \tag{1}$$

$$Re_a = \frac{\rho_a V_{ch,a} L_{ch,a}}{\mu_a} \tag{2}$$

In order to accommodate the effects of gravity and fall height, the characteristic velocity of water ($V_{ch,w}$) was taken to be that of water as it lands on the bottom of the channel in stagnant air. This was not measured directly but estimated using the Bernoulli equation, as shown in Equation 3.

$$V_{ch,w} = \sqrt{{V_{m,w}}^2 + 2gH_f} \tag{3}$$

The characteristic length of a water sheet for the “flow” Weber number has previously been reported to be half the thickness of the water sheet at the nozzle exit [18], whereas, in this study, in order to accommodate the effects of fall height, the “local” Weber number was considered. For this, the sheet thickness at the bottom of the channel was determined, assuming that there is no crossing airflow and the water sheet spanned the full width of the duct. Half of this thickness, as shown in Equation 4, is taken to be the characteristic length as used in the literature [18].

$$L_{ch,w} = \frac{A_{loc,w}}{2W_{noz}} \tag{4}$$

The shape and extent of the sheet of the falling water influences the Reynolds number of the air crossflow, by their effect on the cross-sectional area of the air stream. As such, higher water flow rates result in larger blockage ratios, which consequently increases the velocity of air by reducing the cross sectional area. Therefore, in the determination of the Reynolds number, the average velocity was considered to be a characteristic velocity as defined in Equation 5.

$$V_{ch,a} = V_{m,a} - V_R \tag{5}$$

Where, the resultant velocity (V_R) can be determined by Equation 6.

$$V_{\mathrm{R}} = \frac{\dot{m}_a V_{m,a}}{\dot{m}_a + \dot{m}_w} \tag{6}$$

In order to accommodate the influence of fall height and channel width simultaneously on the Reynolds number, the characteristic length ($L_{ch,a}$) of the gas stream in Equation 2, was chosen to be the diagonal of the duct.

A series of experiments were performed in order to characterise and map the different flow regimes in a crossflow interaction of ducted air with falling sheets of water. In these tests, the airflow rate was varied to provide a range of Reynolds numbers between 5000 and 25000, and the water flow rates was changed to provide a variety of Weber numbers from 1.5 to 7. Figure 8 illustrates the flow regime map based on the Reynolds number of air and the Weber number of water as described.

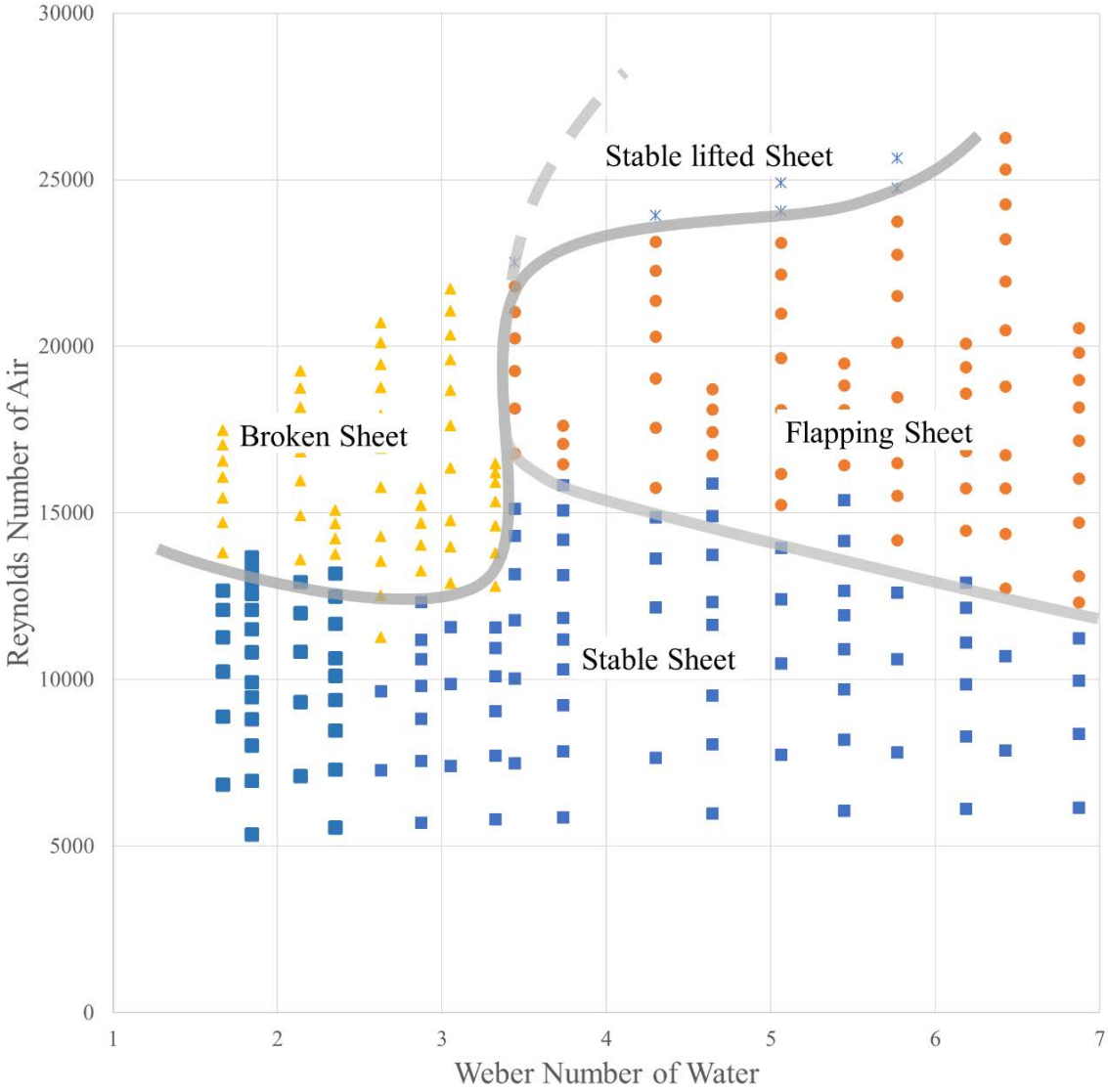

Figure 8. Flow regime map

It was observed that for the entire range of examined Weber numbers and at lower Reynolds number, the sheet of water was stable. The critical Reynolds number for “stable sheets” was seen to be around 12500 beyond which, depending on the Weber number of water,

the stable sheet was transformed to either a “broken sheet” or “flapping sheet”. In the range examined, the critical Weber number was seen to be around 3.5, below this value the flow regime was found to be “broken”, and beyond that the “flapping sheet” was observed. A second critical Reynolds number of approximately 22500 was also observed, beyond which the “flapping sheet” was transformed to a “stable lifted sheet”.

4. Formulating the transfer Processes

In order to be able to generalise heat and mass transfer processes to the design of heat and mass exchangers they should be formulated in dimensionless terms. Nusselt and Sherwood numbers are the representative dimensionless numbers used to describe the heat and mass transfer phenomenon, respectively. In consideration of the mass transfer process, the Sherwood number is defined by Equations 7.

$$Sh = \frac{jL_{ch}}{\lambda_{a-w}} \tag{7}$$

Where, the mass transfer coefficient (j) can be found from Equation 8.

$$j = \frac{\dot{m}_{ev}}{A\left(\rho_{v,f} - \rho_{v,\infty}\right)} \tag{8}$$

The rate of evaporation ($\dot{m}_{ev}$) in Equation 8, is determined from the change in specific humidity as shown in Equation 9.

$$\dot{m}_{ev} = \dot{m}_a(\omega_{a,out} - \omega_{a,in}) \tag{9}$$

And assuming water vapour as an ideal gas, the vapour density (ρ_v) can be calculated from Equation 10.

$$\rho_v = \frac{P_v}{R_v T} \tag{10}$$

On the heat transfer side, the experimental value of Nusselt number is defined by Equation 11.

$$Nu = \frac{hL_{ch}}{k_a} \tag{11}$$

Where the heat transfer coefficient (h) can be determined from Equation 12.

$$h = \frac{\dot{Q}_{conv}}{A\left(T_f - T_\infty\right)} \tag{12}$$

In which, the film temperature (T_f) is the mean temperature of air and water streams.

The effect of radiation heat transfer is neglected, therefore, the rate of convective heat transfer ($\dot{Q}_{conv}$) can be determined from Equation 13.

$$\dot{Q}_{conv} = \dot{Q}_t - \dot{Q}_{ev} \tag{13}$$

Where, the rate of total heat transfer ($\dot{Q}_t$) and the rate of evaporative heat transfer ($\dot{Q}_{ev}$) are given in Equations 14 and 15, respectively.

$$\dot{Q}_t = \dot{m}_a(\hbar_{a,out} - \hbar_{a,in}) \tag{14}$$

$$\dot{Q}_{ev} = \dot{m}_{ev}\hbar_{fg} \tag{15}$$

4.1. Dimensional Analysis

For many simple forced convection processes, the Nusselt number is a function of the Reynolds number and the Prandtl number as given in Equation 16 [33],

$$Nu = f(Re, Pr) \tag{16}$$

The Sherwood number is governed by the Reynolds and Schmidt numbers, as given in Equation 17 [33].

$$Sh = f(Re, Sc) \tag{17}$$

In more complex conditions, the Nusselt number might be governed by some other dimensionless groups in addition to the Reynolds and Prandtl numbers [34-37]. Similarly, the Sherwood number might be defined with some other dimensionless groups besides the Reynolds and Schmidt numbers [38, 39]. Therefore, the Buckingham π theorem was employed in order to identify the effective dimensionless groups in the particular circumstances of a falling sheet of water crossed by a ducted airflow. This analysis delivered eight independent dimensionless groups, as shown in Table 2.

Table 2. Independent dimensionless groups

$\pi_1 = \frac{L_{ch}h}{k_a}$	$\pi_3 = \frac{\rho_a V_{ch} L_{ch} cp_a}{k_a}$	$\pi_5 = \frac{\lambda_{a-w}}{V_{ch} L_{ch}}$	$\pi_7 = \frac{\hbar_{fg}}{{V_{ch}}^2}$
$\pi_2 = \frac{\mu_a}{\rho_a V_{ch} L_{ch}}$	$\pi_4 = \frac{k_a \Delta T}{\rho_a {V_{ch}}^3 L_{ch}}$	$\pi_6 = \frac{j}{V_{ch}}$	$\pi_8 = \frac{\hbar_f}{{V_{ch}}^2}$

Traditional dimensionless groups were identified as follow: π_1 is the Nusselt number (*Nu*), π_2^{-1} is the Reynolds number (*Re*), π_3 is the Peclet number (*Pe*), π_5^{-1} is the Bodenstein (*Bd*) or mass Peclet (Pe_m) number and π_7^{-1} is the Evaporation number (N_{ev}). Grouping π_2 and π_3 delivers the Prandtl number (*Pr*) and combination of π_2 and π_5 gives the Schmidt number (*Sc*).

As seen in Table 2, some new dimensionless group were also identified as follow: π_4 is the ratio of sensible heat transfer to the inertia of the air stream and π_6 is the ratio of the mass transfer coefficient to the characteristic velocity. π_8 is the ratio of the enthalpy content of water at film condition to the kinetic energy of the air stream, which can be considered as both a heat and mass transfer related dimensionless groups.

It should be highlighted that the Weber number used for mapping the flow regime, is the ratio of flow inertia to the surface tension, which characterises the mechanics of the fluid and not the heat and mass transfer, so does not feature in the analysis.

5. Results: Heat and Mass Transfer Correlation

Based on the measurements made during the experiment, the properties of air and water, the dimensionless parameters defined from the Buckingham π theorem and the heat and mass transfer coefficients were determined for each condition tested. Table 3 shows the conditions of the experiment.

Table 3. Experimental conditions for heat and mass transfer measurements

Nozzle width	(*m*)	*0.1*
Nozzle thickness	(*m*)	*0.0005*
Air flow rate	(m^3/s)	0.42×10^{-2} *to* 2×10^{-2}
Water flow rate	(m^3/s)	2×10^{-5} *to* 5×10^{-5}
Water temperature	(°*C*)	*30 ; 35 ; 40 ; 45*
Fall height	(*m*)	*0.036 ; 0.048*

Correlations of the Nusselt and Sherwood numbers are typically reported in the form of power functions [33]. Based on this, it was attempted to deliver the Nusselt and Sherwood numbers as a power function including the effective dimensionless parameters. In order to define these correlations, a least squares analysis was performed for the Nusselt and Sherwood numbers determined from the experimental data. The succeeding sections detail the analysis undertaken for the different modes of interaction.

5.1. Stable Sheet

Under the conditions of stable sheet, the increase in blockage ratio is very likely to have an improving effect on the heat and mass transfer processes. In this respect the "water to air mass flow ratio" was considered as an effective dimensionless parameter to describe the mass transfer coefficients of a "stable" sheet. Considering this, the correlation for Sherwood number was defined as being a function of mass transfer related dimensionless groups, identified by the Buckingham π theorem and the mass flow ratio, as given in Equation 18.

$$Sh = aRe^{x}Sc^{y}{N_{ev}}^{z}{\pi_8}^{t}\left(\frac{\dot{m}_w}{\dot{m}_a}\right)^{k} \tag{18}$$

Performing a least squares analysis on Equation 18, determines the constants of the correlation shown in Equation 19.

$$Sh = 3.95\times10^{-6}Re^{1.88}Sc^{0.43}{N_{ev}}^{0.43}{\pi_8}^{-0.43}\left(\frac{\dot{m}_w}{\dot{m}_a}\right)^{0.88} \tag{19}$$

This correlation is shown in Figure 9. It is seen that most of the predicted data from the correlation, given in Equation 19 lay within ±25% of the experimental values calculated from Equation 7.

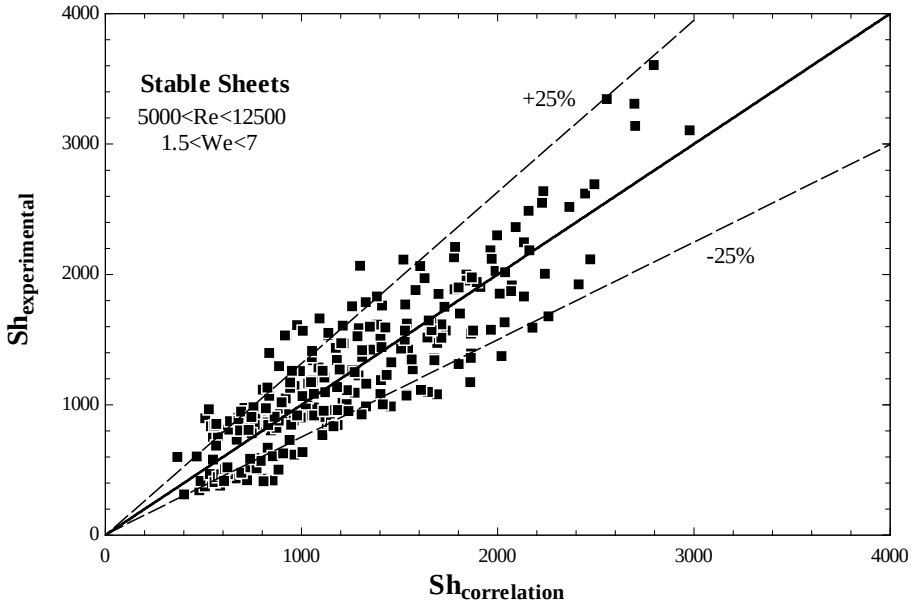

Figure 9. The experimental Sherwood number versus calculated value

As seen in Equation 19, it was found that the exponent of Schmidt and Evaporation numbers are equal and the exponent of π_8 holds the negative value of the exponents of Schmidt and Evaporation numbers. Thus, Equation 19 can be simplified as shown in Equation 20.

$$Sh = 3.95 \times 10^{-6}\, Re^{1.88} \left(\frac{ScN_{ev}}{\pi_8}\right)^{0.43} \left(\frac{\dot{m}_w}{\dot{m}_a}\right)^{0.88} \tag{20}$$

The ratio of Evaporation number and π_8 is in fact the ratio of the enthalpy of evaporation of water to the enthalpy content of air at the film condition, where the air is saturated at the mean temperature of air and water. This ratio will be referred to as the enthalpy ratio in this context, and the product of this ratio and the Schmidt number forms a new dimensionless number, which from hereon will be referred to as the Schmidt Number of Evaporation, as defined in Equation 21.

$$Sc_{ev} = \frac{ScN_{ev}}{\pi_8} = \frac{\frac{\mu_a}{\rho_a \lambda_{a-w}} \frac{\hbar_{fg}}{{V_{ch}}^2}}{\frac{\hbar_f}{{V_{ch}}^2}} = \frac{\nu_a}{\lambda_{a-w}} \frac{\hbar_{fg}}{\hbar_f} = Sc \frac{\hbar_{fg}}{\hbar_f} \tag{21}$$

The Schmidt Number of Evaporation expresses the viscous diffusion and mass diffusion with respect to the required heat of evaporation and the enthalpy content of the bulk stream at the film conditions. This dimensionless number characterises the mass transfer in a low temperature evaporation process.

Based on these, the empirical correlation for the Sherwood number given in Equation 20, can be simplified to Equation 22.

$$Sh = 3.95 \times 10^{-6}\, Re^{1.88} {Sc_{ev}}^{0.43} \left(\frac{\dot{m}_w}{\dot{m}_a}\right)^{0.88} \quad (22)$$

As the Nusselt number is the heat transfer equivalent of the Sherwood number, and since the mechanism of heat and mass transfer are functionally similar, the correlation for Nusselt number is expected to be similar to Sherwood correlation. Therefore, the correlation of Nusselt number was set as a function of heat transfer-related dimensionless groups from the Buckingham π theorem and the mass flow ratio as given in Equation 23.

$$Nu = aRe^{x} Pr^{y} {N_{ev}}^{z} {\pi_8}^{t} \left(\frac{\dot{m}_w}{\dot{m}_a}\right)^{k} \quad (23)$$

Performing a least square analysis on the Nusselt number given in Equation 23, defines the constants of the correlation as given in Equation 24.

$$Nu = 3.95 \times 10^{-6} Re^{1.88} Pr^{0.43} {N_{ev}}^{0.43} {\pi_8}^{-0.43} \left(\frac{\dot{m}_w}{\dot{m}_a}\right)^{0.88} \quad (24)$$

As illustrated in Figure 10 most of data calculated from the correlation given in Equation 24 are within ±25% of the experimental values of the Nusselt number.

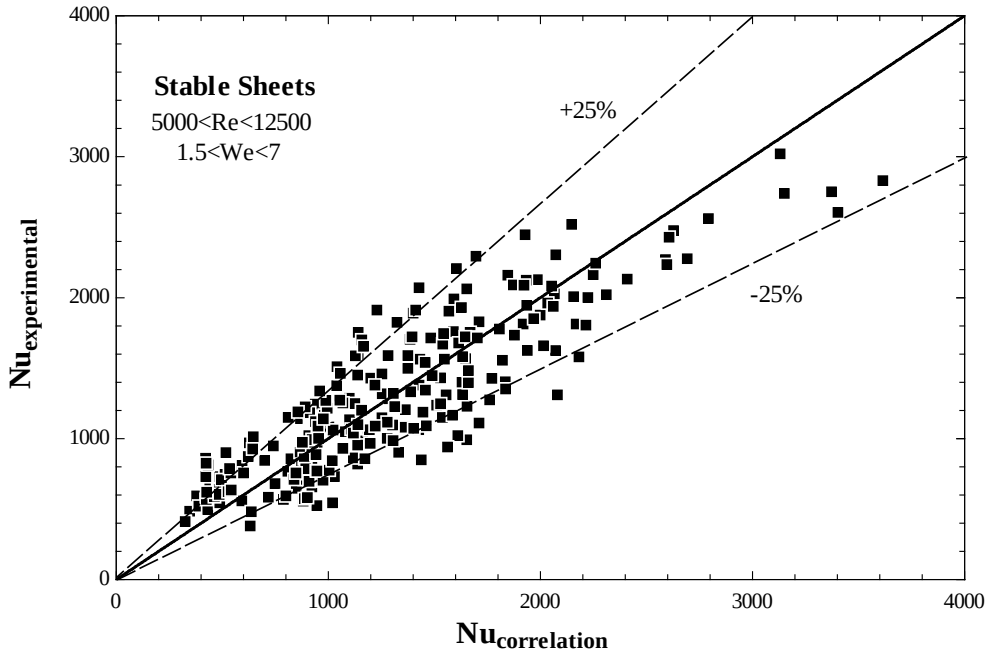

Figure 10. Comparison of Nusselt number with its experimental values

Analogous to the correlation of Sherwood number, the dimensionless groups; π_8, Prandtl and Evaporation numbers can be combined, which reduces Equation 24 to Equation 25.

$$Nu = 3.95 \times 10^{-6}\, Re^{1.88} \left(\frac{PrN_{ev}}{\pi_8}\right)^{0.43} \left(\frac{\dot{m}_w}{\dot{m}_a}\right)^{0.88} \quad (25)$$

The product of Prandtl number and the ratio of π_8 and Evaporation number, as presented in Equation 26, formed a new dimensionless group, herein called the Prandtl Number of Evaporation.

$$Pr_{ev} = \frac{PrN_{ev}}{\pi_8} = \frac{\frac{cp_a\mu_a}{k_a}\frac{\hbar_{fg}}{{V_{ch}}^2}}{\frac{\hbar_f}{{V_{ch}}^2}} = \frac{cp_a\,\mu_a}{k_a}\frac{\hbar_{fg}}{\hbar_f} = Pr\frac{\hbar_{fg}}{\hbar_f} \tag{26}$$

The Prandtl Number of Evaporation expresses the ratio of viscous diffusion to thermal diffusion relative to the enthalpy of vaporization and the enthalpy content of air stream at film conditions. Higher values of this number indicate that viscous diffusion is the dominant mechanism. The ratio of latent heat of vaporization to the heat capacity of the bulk fluid, characterizes the low temperature evaporation processes where the enthalpy of evaporation is significantly higher than that delivered to the system.

Nusselt number has a similar functional form to the Sherwood number and is determined to be a function of Reynolds number and Prandtl Number of Evaporation, as well as the water to air mass flow ratio. Equation 27 is the empirical relation for Nusselt number found from this work.

$$Nu = 3.95 \times 10^{-6}\, Re^{1.88} {Pr_{ev}}^{0.43} \left(\frac{\dot{m}_w}{\dot{m}_a}\right)^{0.88} \tag{27}$$

5.2. Broken Sheet

A broken sheet was formed at relatively low water flow and high airflow rates, which, compared to stable sheets, the water sheet has a very small effect on the cross-sectional area of air stream. Due to the narrow range of water flow rate under the circumstances of broken sheets, the mass flow rate of water and consequently mass flow ratio was found to be practically ineffective on the mass transfer. Therefore the functional form of the Sherwood number was taken to be a function of the mass transfer related dimensionless groups from the Buckingham π theorem, as given in Equation 28.

$$Sh = aRe^x Sc^y {N_{ev}}^z {\pi_8}^t \tag{28}$$

By performing a least squares analysis, the constants of the correlation was determined which defined the Sherwood number as shown in Equation 29.

$$Sh = 0.00035\, Re^{2.9} Sc^{2.9} {N_{ev}}^{0.912} {\pi_8}^{-0.000335} \tag{29}$$

As illustrated in Figure 11, most of the calculated results from the empirical correlation given by Equation 29 are within ±25% of the experimental values of Sherwood number.

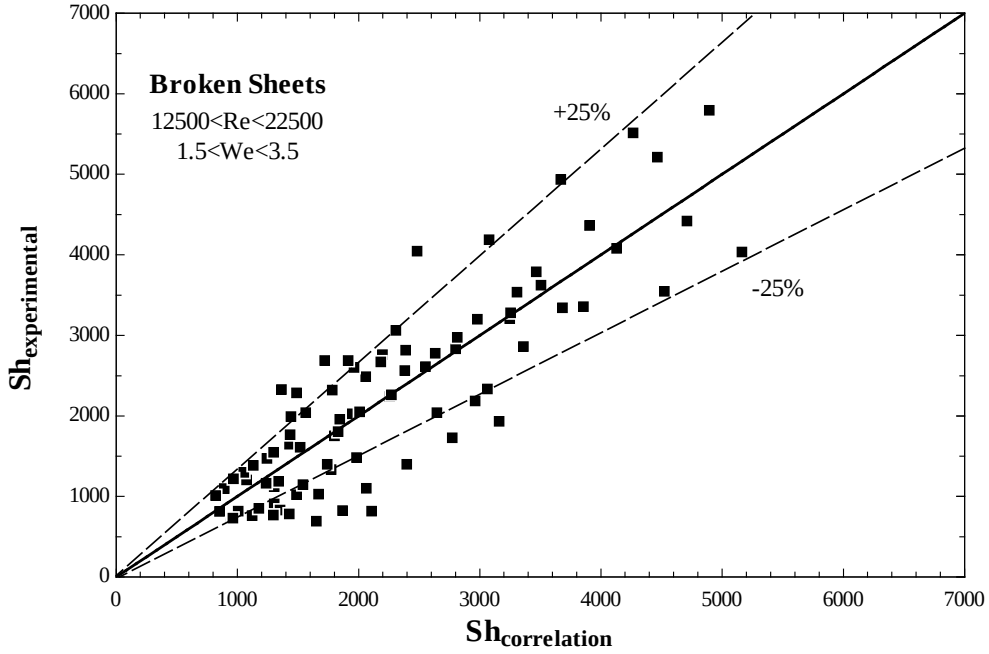

Figure 11. Experimental Sherwood number versus the corresponding values from the empirical correlation

As expected, the exponents of Reynolds and Schmidt numbers, in Equation 29, are equal and are combined to form the Bodenstein Number (mass transfer Peclet number). The very small exponent of π_8 suggests that; in the range tested, this number does not affect the value of Sherwood number and can be excluded from the correlation. Hence, Equation 29 can be simplified to Equation 30.

$$Sh = 0.00035\, Bd^{2.9} {N_{ev}}^{0.912} \tag{30}$$

This can be explained by the fact that in a broken sheet, the water sheet breaks into smaller fingers or droplets, and since the airflow is considerably higher than the water flow rate, the water temperature drops rapidly to the wet bulb temperature of air as a result of evaporative cooling. Under these circumstances, the film temperature would be the wet bulb temperature of the air stream. Therefore, the main mechanism of mass transfer would be through advection, which can be described by the Bodenstein number. On the other hand, some of the mass transfer is taking place as a result of sheet breakup by the air stream through viscous diffusion, where the driving force is the kinetic energy of the air stream.

Analogous to the Sherwood number, the Nusselt number was determined to be a function of the Peclet number, which is the equivalent of the Bodenstein number in heat transfer, and the Evaporation number. Due to the heat and mass transfer analogy, the functional form of the Nusselt number is similar to that describing Sherwood number and is given by Equation 31.

$$Nu = 0.00035\, Pe^{2.9} {\mathrm{N}_{ev}}^{0.912} \tag{31}$$

As shown in Figure 12, most of the calculate data from Equation 31 are within ±25% of the experimental values of the Nusselt number.

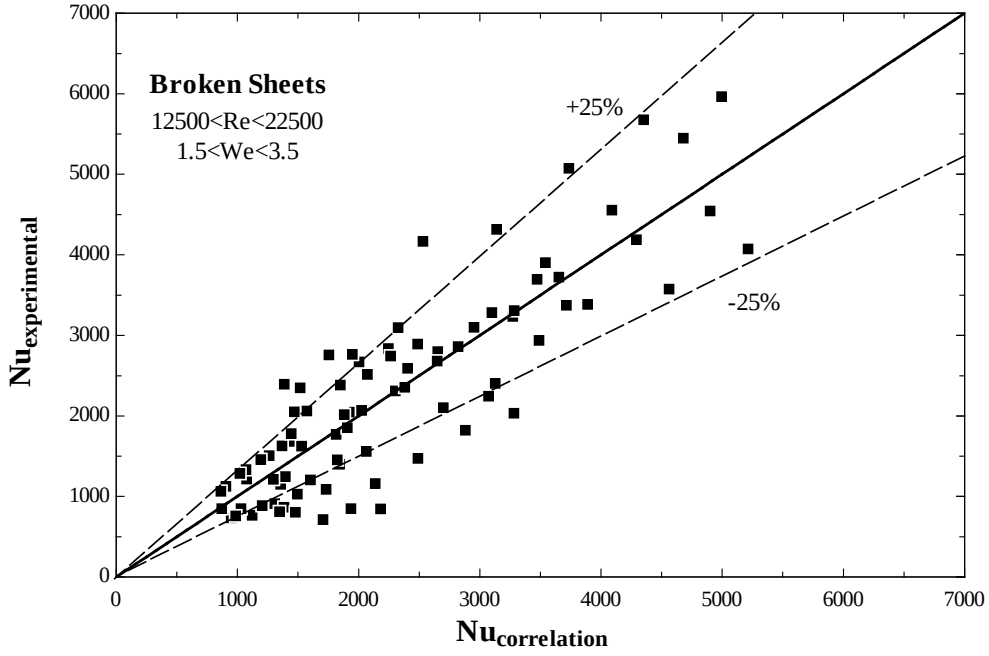

Figure 12. Experimental Nusselt number versus the corresponding calculated values.

5.3. Flapping Sheet

As a result of high flow rates of water, the mechanism of heat and mass transfer under the conditions of flapping sheets is similar to stable sheets. However, due to the flapping nature of this flow regime the blockage ratio changes continuously. This makes the cross sectional area of airflow independent of the water flow rate and as a consequence, the mass flow ratio was found to have little influence on the Sherwood number. Therefore, the initial correlation of Sherwood number was written as a function of mass transfer related dimensionless groups from the Buckingham π theorem, as shown in Equation 32.

$$Sh = aRe^{x}Sc^{y}{N_{ev}}^{z}{\pi_8}^{t} \tag{32}$$

A least squares analysis was used to determine the constants of the correlation, which resulted in Equation 33.

$$Sh = 4.78 \times 10^{-8} Re^{2.23} Sc^{1.175} {N_{ev}}^{1.175} {\pi_8}^{-1.175} \tag{33}$$

Similar to the correlation of the Sherwood number for the stable sheets, the exponent of Schmidt and Evaporation numbers are equal and the exponent of π_8 holds the negative value of the exponents of Schmidt and Evaporation numbers. Therefore, the Sherwood number correlation for flapping sheets can be represented as a function of the Reynolds and Schmidt Number of Evaporation as shown in Equation 34.

$$Sh = 4.78 \times 10^{-8}\, Re^{2.23} {Sc_{ev}}^{1.175} \tag{34}$$

Shown in Figure 13 is a comparison of the predicted values of the Sherwood number from Equation 34 with the experimental values. It is seen that most of the predicted values, are within a range of ±30% of the experimental values.

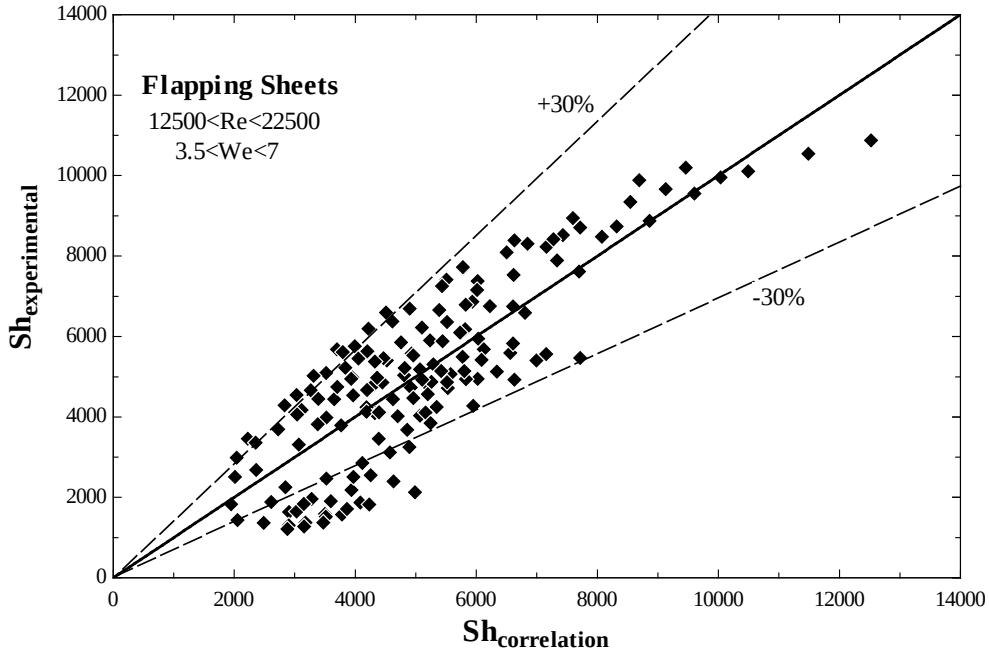

Figure 13. Experimental Sherwood versus the correlation for flapping sheet

In consideration of the heat transfer in flapping sheets, analogous to Sherwood number, the correlation for Nusselt number was initially set to be a function of the heat transfer-related dimensionless groups from the Buckingham π theorem as shown in Equation 35.

$$Nu = aRe^{x}Pr^{y}{N_{ev}}^{z}{\pi_8}^{t} \tag{35}$$

As given in Equation 36, the constants of the correlation given in Equation 35, were defined by performing a least squares analysis.

$$Nu = 4.78 \times 10^{-8}Re^{2.23}Pr^{1.175}{N_{ev}}^{1.175}{\pi_8}^{-1.175} \tag{36}$$

Shown in Figure 14 is the comparison of the predicted values of Nusselt number from the correlation given in Equation 36 with the experimental values of Nusselt number which, most of the calculated data are within ±30% from the experimental values.

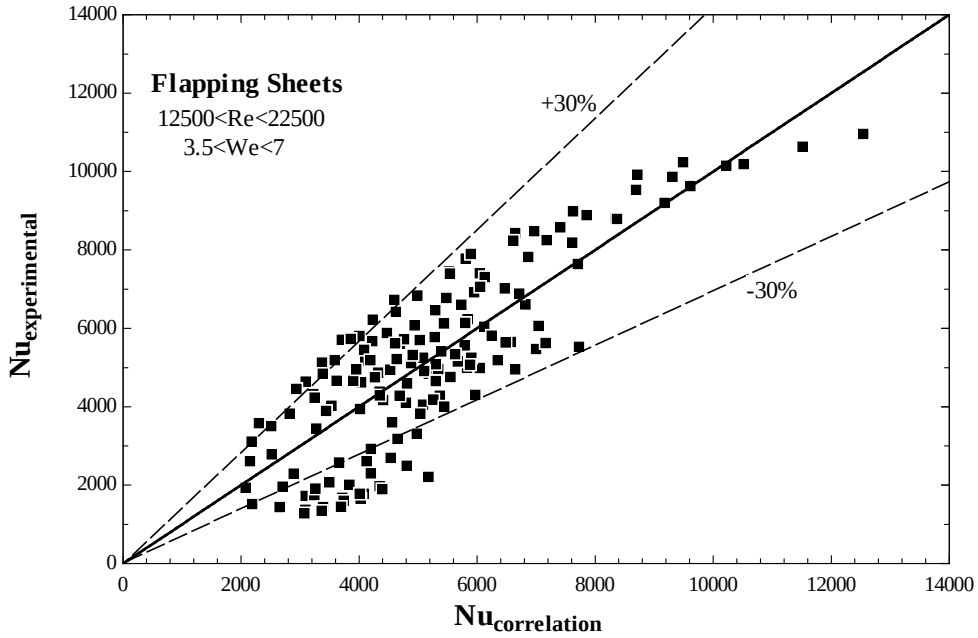

Figure 14. Comparison of the correlation of Nusselt number with the experimental values

It was seen in Equation 36 that the exponents of Prandtl and Evaporation numbers are equal and the exponent of π_8, holds the negative value of the exponent of Prandtl and Evaporation numbers. Therefore, the correlation of Nusselt number for flapping sheets can be defined as a function of the Reynolds number and the Prandtl Number of Evaporation, as shown in Equation 37.

$$Nu = 4.78 \times 10^{-8}\, Re^{2.23} {Pr_{ev}}^{1.175} \tag{37}$$

6. Conclusion

An experimental investigation was performed in order to first identify and map the existing flow regimes in a crossflow interaction of air and falling sheets of water and from this formulate the intensities of heat and mass transfer for each flow regimes. In this respect, the Buckingham π theorem was used to identify the dimensionless groups governing the problem. Subsequently, the least squares analysis was performed to determine the correlations of the Nusselt and Sherwood numbers as a function of the dimensionless numbers from the Buckingham π theorem. This has led to introduction of a new dimensionless parameters that characterise the transfer phenomena in low temperature evaporation processes with crossflow interaction. This parameter was defined as the ratio of the enthalpy of evaporation and the enthalpy of the air at film condition, which was referred to as the enthalpy ratio. In considering the heat transfer process, the product of this parameter and the Prandtl number gave rise to a new dimensionless number which was named Prandtl Number of Evaporation. Similarly, on the mass transfer side, the Schmidt Number of Evaporation was defined as a product of the Schmidt number and the enthalpy ratio. It was found that between the three modes of interaction, “Flapping” mode is the strongest and “Stable” mode is the weakest flow regime, in terms of intensities of heat and mass transfer.

7. References

[1] R. Enayatollahi, T. Anderson, R. Nates, Mathematical modeling of a solar powered humidification dehumidification desalination prototype, in: Solar 2014: The 52nd Annual Conference of the Australian Solar Council, Solar 2014 Conference & Expo, Melbourne, 2014.

[2] P. Naphon, Study on the heat transfer characteristics of an evaporative cooling tower, International Communications in Heat and Mass Transfer, 32 (2005) 1066-1074.

[3] V.D. Stevanovic, An analytical model for gas absorption in open-channel flow, International Communications in Heat and Mass Transfer, 24 (1997) 1187-1194.

[4] A. Klimanek, R.A. Biatecki, , Solution of heat and mass transfer in counterflow wet-cooling tower fills, International Communications in Heat and Mass Transfer, 36 (2009) 547–553.

[5] Z. Huang, P. Jiang, Theoretical Analysis and Numerical Simulation of Coupled Relationship of Heat and Mass Transfer Between Air and Desiccant in Liquid Desiccant Dehumidification, in: Proceedings of the 8th International Symposium on Heating, Ventilation and Air Conditioning, Springer, 2014, pp. 829-839.

[6] U. Ullah, S.P. Waldram, C.J. Bennett, T. Truex, Monolithic reactors: mass transfer measurements under reacting conditions, Chemical Engineering Science, 47(9–11) (1992) 2413-2418.

[7] S. Eiamsa-ard, C. Thianpong, P. Promvonge, Experimental investigation of heat transfer and flow friction in a circular tube fitted with regularly spaced twisted tape elements, International Communications in Heat and Mass Transfer, 33(10) (2006) 1225-1233.

[8] V.I. Deshko, A.Y. Karvatskii, I.O. Sukhodub, Heat and mass transfer in cross-flow air-to-air membrane heat exchanger in heating mode, Applied Thermal Engineering, 100 (2016) 133-145.

[9] J.H. Lee, G.H. Ro, Y.T. Kang, Y.S. Chang, S.C. Kim, Y.L. Kim, Combined heat and mass transfer analysis for LiCl dehumidification process in a plate type heat exchanger, Applied Thermal Engineering, 96 (2016) 250-257.

[10] S.W. Churchill, M. Bernstein, A Correlating Equation for Forced Convection From Gases and Liquids to a Circular Cylinder in Crossflow, Journal of Heat Transfer, 99(2) (1977) 300-306.

[11] H.K. Wee, R.B. Keey, M.J. Cunningham, Heat and moisture transfer by natural convection in a rectangular cavity, International Journal of Heat and Mass Transfer, 32(9) (1989) 1765-1778.

[12] C.R. Iskra, C.J. Simonson, Convective mass transfer coefficient for a hydrodynamically developed airflow in a short rectangular duct, International Journal of Heat and Mass Transfer, 50(11–12) (2007) 2376-2393.

[13] S.-H. Sun, T.R. Marrero, Experimental study of simultaneous heat and moisture transfer around single short porous cylinders during convection drying by a psychrometry method, International Journal of Heat and Mass Transfer, 39(17) (1996) 3559-3565.

[14] W. Chuck, E.M. Sparrow, Evaporative mass transfer in turbulent forced convection duct flows, International Journal of Heat and Mass Transfer, 30(2) (1987) 215-222.

[15] L.W. Casperson, Fluttering fountains, Journal of Sound and Vibration, 162 (1991) 251-262.

[16] L.W. Casperson, Fluttering fountains: Annular geometry, Journal of Applied Physics, 79 (1996) 1275-1278.

[17] D.L. Chubb, F.D. Calfo, M.W. McConley, M.S. McMasters, A.A. Afjeh, Geometry of thin liquid sheet flows, AIAA Journal, 32 (1994) 1325-1328.

[18] L.D. Luca, Experimental investigation of the global instability of plane sheet flows, Journal of Fluid Mechanics, 399 (1999) 355-376.

[19] P.J. Schmid, D.S. Henningson, On the stability of falling liquid curtain, Journal of Fluid Mechanics, 463 (2002) 163-173.

[20] J.O. Marston, S.T. Thoroddsen, J. Thompson, M.G. Blyth, D. Henry, J. Uddin, Experimental investigation of hysteresis in the break-up of liquid curtains, Chemical Engineering Science, 117 (2014) 248-263.

[21] H. Kyotoh, K. Fujita, K. Nakano, T. Tsuda, Flow of a falling liquid curtain into a pool, Journal of Fluid Mechanics, 741 (2014) 350-376.

[22] A.A. Ibrahim, M.A. Jog, Nonlinear instability of an annular liquid sheet exposed to gas flow, International Journal of Mutiphase Flow, 34 (2008) 674-664.

[23] J. Mazzallon, Z. Dai, G.M. Faeth, Primary breakup of nunturbulent round liquid jets in gas crossflows, Journal of Atomization and Sprays, 9 (1999) 291-312.

[24] J.M. Gordillo, M. Perez-Saborid, Aerodynamic effects in the break-up of liquid jets: on the first wind-induced break-up regime, Journal of Fluid Mechanics, 541 (2005) 1-20.

[25] R. Bolanos-Jimenez, A. Sevilla, C. Gutierrez-Montes, E. Sanmiguel-Rojas, C. Martinez-Bazan, Bubbling and jetting regimes in planar coflowing air-water sheets, Journal of Fluid Mechanics, 668 (2011) 519-542.

[26] C.-L. Ng, R. Snakarakrishnan, K.A. Sallam, Bag breakup of nontirbulent liquid jets in crossflow, International Journal of Multiphase Flow, 34 (2008) 241-259.

[27] D.R. Brown, A study of the behaviour of thin sheet of moving liquid, Journal of Fluid Mechanics, 10 (1961) 297-305.

[28] M. Becerra, M.S. Carvalho, Stability of viscoelastic liquid curtain, Chemical Engineering and Processing: Process Intensification, 50 (2011) 445-449.

[29] P. Spedding, D. Spence, Flow regimes in two-phase gas-liquid flow, International journal of multiphase flow, 19(2) (1993) 245-280.

[30] D. Barnea, O. Shoham, Y. Taitel, Flow pattern transition for vertical downward two phase flow, Chemical Engineering Science, 37(5) (1982) 741-744.

[31] A.A. Kendoush, S.A. Al-Khatab, Experiments on flow characterization in vertical downward two-phase flow, Experimental thermal and fluid science, 9(1) (1994) 34-38.

[32] T. Furukawa, T. Fukano, Effects of liquid viscosity on flow patterns in vertical upward gas–liquid two-phase flow, International Journal of Multiphase Flow, 27(6) (2001) 1109-1126.

[33] Y.A. Cengel, Heat and Mass Transfer, 3rd ed., New York: McGraw-Hill, 2007.

[34] D. Metzger, L. Florschuetz, D. Takeuchi, R. Behee, R. Berry, Heat transfer characteristics for inline and staggered arrays of circular jets with crossflow of spent air, Journal of Heat Transfer, 101(3) (1979) 526-531.

[35] M.A. Habib, A.M. Attya, S.A.M. Said, A.I. Eid, A.Z. Aly, Heat transfer characteristics and Nusselt number correlation of turbulent pulsating pipe air flows, Heat and Mass Transfer, 40(3) (2004) 307-318.

[36] S.K. Saini, R.P. Saini, Development of correlations for Nusselt number and friction factor for solar air heater with roughened duct having arc-shaped wire as artificial roughness, Solar Energy, 82(12) (2008) 1118-1130.

[37] A.S. Gbadebo, M.S.A. Said, A.M. Habib, Average Nusselt number correlation in the thermal entrance region of steady and pulsating turbulent pipe flows, Heat and Mass Transfer, 35(5) (1999) 377-381.

[38] T.W. Chung, H. Wu, Mass Transfer Correlation for Dehumidification of Air in a Packed Absorber with an Inverse U-Shaped Tunnel, Separation Science and Technology, 35(10) (2000) 1503-1515.

[39] Y.T. Kang, A. Akisawa, T. Kashiwagi, Experimental correlation of combined heat and mass transfer for NH3–H2O falling film absorption, International Journal of Refrigeration, 22(4) (1999) 250-262.